



Department of Biomedical Engineering  
Soft Tissue Biomechanics & Tissue Engineering Research Group

# Excessive Skin Folding & Skin Appendages: A Finite Element Model

*Bachelor Thesis*

Souren, L.H.F. (sn.1339133)

Supervisors:

dr. ir. Loerakker, S. superior supervisor  
MSc. Ralvoni, J. daily supervisor

Eindhoven, 23rd of June 2021

# Abstract

Excessive skin folding, the process of skin layers folding in ptotic envelopes after heavy weight loss, is a more than common complaint of post-obesity patients after bariatric surgery (Björserud et al., 2013), or intensive diets. With increasing numbers of obesity patients worldwide (numbers that even reach epidemic proportions), simultaneously, a rising trend in bariatric surgical procedures has emerged (Atiyeh and Castagliola, 2012). The increase of excessive skin folding complaints is, thus, not that surprising. The folds are not only clumsy and annoying in physical activities, but are generally unattractive as well, reducing the quality of life (Song et al., 2006; Toma et al., 2018).

Cortical folding examples in literature, with similar folding morphology, relate small perturbations (or imperfections) to cause different top surface folding morphologies in an already folded material (Garcia et al., 2018), but also relate them to trigger the folding of a material that does not fold either way (Garcia et al., 2018; Wang et al., 2021). In both circumstances, the imperfections lower the potential energy of the system (Mavrodontis, 2017). The question arose whether skin appendages (or skin non-linearities) such as hair follicles and sweat glands can behave as model imperfections in finite element models, and thus, can change the outcome of the folding process. Results of *in vitro* experiments regarding skin non-linearities (Szabo, 1967; Wilke et al., 2007; Wosicka and Cal, 2010) show that the skin non-linearities differ significantly in depth, diameter and distribution (numbers per surface area) on the skin. An interest, thus, emerged in the influence of depth and quantity of the skin non-linearities on the excessive skin folding.

A total of thirteen simulations were performed using a finite element model in Abaqus/Explicit (Abaqus/Explicit, 2021). In the simulations, type of skin non-linearity and quantity of these skin non-linearities were varied. The skin non-linearities, non-visible vellus hair follicles, visible terminal hair follicles, and sweat glands were applied as imperfections. The imperfections were implemented as nodal displacements at random locations on the model's top surface. The normalized mean curvature  $\kappa^*$  (or sharpness of the folding) in the final state of the integration points was used to quantify the results. It was concluded from the final state of the simulations, that the presence of any single skin non-linearity results in a different top surface morphology of the folding, compared to the top surface morphology in the control group with no implemented imperfection. This is in accordance with the hypothesis based on Garcia et al. (2018).

The depth of the skin non-linearity, however, has no effect on the folding, as no convincing difference in  $\kappa^*$  has been found between the different single skin non-linearities. The same conclusion holds for the simulations with different quantities of implemented skin non-linearities. Top surface morphologies of these simulations appeared to be similar to either the ones seen in the single skin non-linearity simulations, or the one seen in the control group simulation. In accordance with these visible simulation results, no dependency of the quantity of skin non-linearities  $\kappa^*$  was found.

Furthermore, it was concluded that the skin non-linearities, independent of which depth and quantity simulated, do not lower the critical folding stress  $\sigma_{xx}$  of the skin. The results indicated, nevertheless, a dependency between the location of the skin non-linearity, and the top surface morphology in the final state of the folding. The location is not researched extensively in this report, which thus lacks evidence to draw any conclusions on that part. An organized placement of the nodes based on abdominal hair distributions typically seen in both female and male (Setty, 1966, 1967; Zickler, 1997) might provide some interesting results after further research.

# Contents

<b>Contents</b>	<b>iii</b>
<b>1 Introduction</b>	<b>1</b>
<b>2 Methods</b>	<b>5</b>
2.1 The benchmark model . . . . .	5
2.1.1 One-element model setup . . . . .	5
2.1.2 Analytical solution of the one-element benchmark model. . . . .	6
2.1.3 Multiple element benchmark model . . . . .	8
2.2 Bi-layered, multiple element model of the dermis and hypodermis. . . . .	10
2.3 Implementation of skin non-linearities. . . . .	11
2.3.1 Method of implementing the imperfection . . . . .	12
2.3.2 Determining the number of imperfection nodes . . . . .	13
2.3.3 Terminal hair count using the Ferriman & Gallwey score . . . . .	13
2.4 Quantifying the results: normalized mean curvature $\kappa^*$ . . . . .	14
<b>3 Results</b>	<b>15</b>
3.1 Control group & one imperfection simulations . . . . .	15
3.2 Mean distribution of skin non-linearities simulations . . . . .	18
3.3 Varying Ferriman & Gallwey score simulations . . . . .	19
<b>4 Discussion</b>	<b>20</b>
<b>5 Conclusions</b>	<b>23</b>
<b>Bibliography</b>	<b>25</b>
<b>Appendix</b>	<b>27</b>

<b>A</b>	<b>Model validations</b>	<b>28</b>
A.1	Benchmark model: Von Mises stress comparison . . . . .	28
A.2	Bi-layered model: Element size check . . . . .	29
A.3	Bi-layered model: Length scale check . . . . .	29
A.4	Validation of curvature quantification model . . . . .	31

# Chapter 1: Introduction

Heavy weight loss, be it as the result of a disciplined diet combined with regular exercise, or as a result of bariatric surgery, improves on people's quality of life (Song et al., 2006). However, losing the weight itself is not the last challenge obesity patients will have to endure. One of the most troubling side effects of heavy weight loss is excessive (or loose) skin, folded in ptotic envelopes. This excessive skin can not only lead to problems in physical function of the patient, but to insecurities about physical appearance as well. Surveys showed that quality of life improves significantly after bariatric surgery, but has to be enhanced by an additional body contouring procedure to obtain the most satisfying results (Song et al., 2006; Toma et al., 2018). Worldwide, an increasing number of obesity patients (leading to even epidemic proportions according to Atiyeh and Castagliola (2012)), and consequently, bariatric surgeries have been observed (Atiyeh and Castagliola, 2012). Understanding the excessive skin folding can be vital information for a surgeon in order to apply the best, patient specific treatment with the least amount of surgical intervention.

No research has been done in understanding the mechanical underlying principles of excessive skin folding yet, despite numerous studies into skin wrinkling for cosmetic purposes ((Shiihara et al., 2015; Leyva-Mendivil et al., 2015)). However, folding with final morphologies similar to excessive skin folding can be found in growth of the cortical layers of the brain. This cortical folding, in contrast to the excessive skin folding, has been extensively studied over the years. Several theories have been proposed (and rejected) with the *differential growth theory* (Bayly et al., 2013; Tallinen et al., 2014) becoming more and more convincing. The theory states that a difference in growth rates between the top (cortex) layer and bottom (subcortex) layer leads to a tangential compression, which, if reached a critical value, can lead to folding of the top layer. The mechanical stiffness ratio between the top and bottom layer alters the morphology of the top layer folding. In the unstable state that occurs before the start of the folding, a small imperfection (or geometrical non-linearity) in the adjacent tissue layers can trigger the start of the folding (if it did not start by itself) (Garcia et al., 2018; Wang et al., 2021), or it can alter the final outcome of the existing folding (Garcia et al., 2018). In both scenarios, the imperfection lowers the potential energy of the system (Mavrodontis, 2017). Especially these small imperfections are of interests in skin mechanics. The skin layers, namely the epidermis, dermis and hypodermis (Figure 1.1), give home to several biological components such as sweat glands, hair follicles, nerves and blood vessels (Marieb and Hoehn, 2015) that can serve as imperfections.

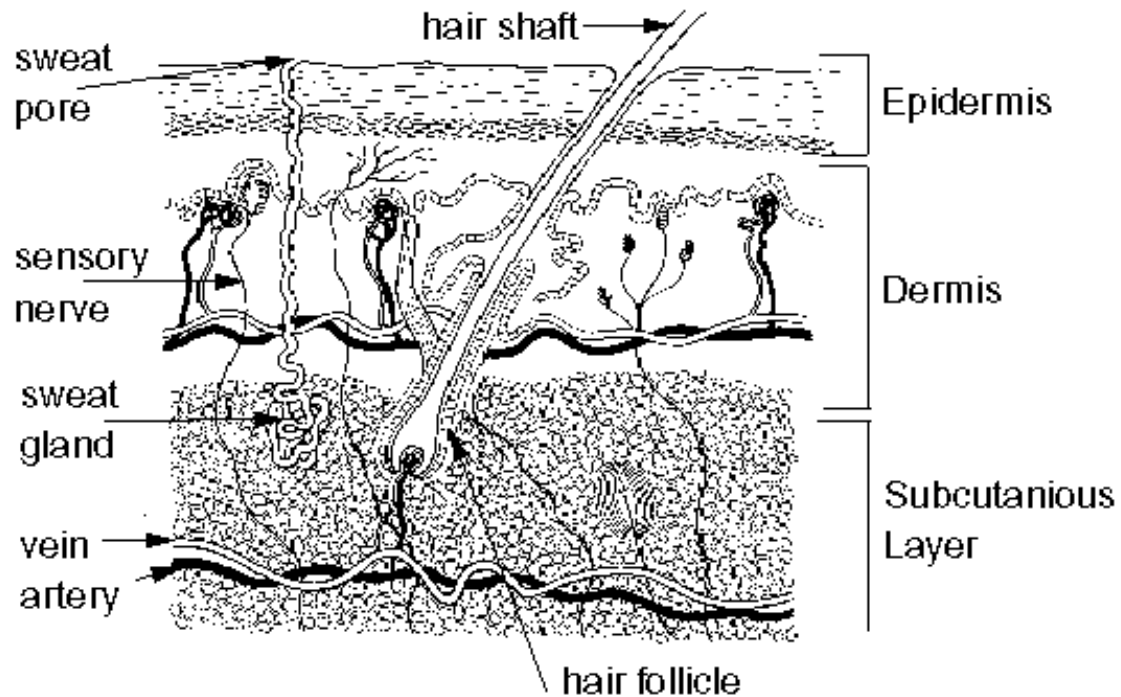


**Figure 1.1: Schematic of the skin layers and fat layer supplemented with skin non-linearities.** Note that the hypodermis is not listed separately in this graph but is referred to as the *subcutaneous layer*. Schematic retrieved from Cotterill (1996).

The top layer of the skin is the epidermis, which consists of both a layer with non-viable (strata corneum), and viable cells (viable epidermis) (Oomens et al., 2017). The epidermis has the largest mechanical stiffness of the skin layers in terms of Young's Modulus  $E$  (Shiihara et al., 2015). But, is not modelled in this report due to its relatively small thickness in the skin compared to the dermis and hypodermis (Shiihara et al., 2015). The second skin layer is the dermis, which is composed of a gel-like matrix containing glycosaminoglycans (GAGS), giving the dermis visco-elastic properties (Oomens et al., 2017). High dense networks of collagen and elastin fibers (Oomens et al., 2017) are embedded in this matrix. Furthermore, these fibers cause the dermis to have anisotropic mechanical properties (Annaidh et al., 2012). The combination of these mechanical properties, and the relatively large thickness of the dermis in the skin make the dermis by far the most frequently modelled skin layer in previous papers studying skin mechanics (Oomens et al., 2017). For this reason, the dermis layer was implemented in the model of this report. However, visco-elastic properties were ignored, and the dermis was assumed to be isotropic for simplicity. The hypodermis layer underlying the skin is mainly composed of loose, fatty tissue (Oomens et al., 2017). Fatty (or adipose) tissue is closely packed with adipocytes (fat cells) with their nuclei pushed to the side by large fat droplets (Marieb and Hoehn, 2015), making the tissue a soft substrate. The gel-matrix of the adipose tissue does contain collagen and elastin fibers, but in sparser amount compared to other connective tissues (Marieb and Hoehn, 2015). Research into the mechanical properties of the hypodermis, or adipose tissue in general, is scarce. However, due to the gel-like matrix, and fibers embedded into the matrix, it is assumed that the hypodermis has similar mechanical properties as the dermis, only with a lower Young's Modulus  $E$  (Shiihara et al., 2015). To mimic the biological multi-layered structure of the skin, the hypodermis was implemented in the model as well under the same simplifications as mentioned earlier for the dermis.

The focus of this report is on the role of skin non-linearities in the excessive skin folding process,

and then in particular the role of sweat glands and hair follicles (both vellus (non-visible) and terminal (visible)) shown in Figure 1.2.

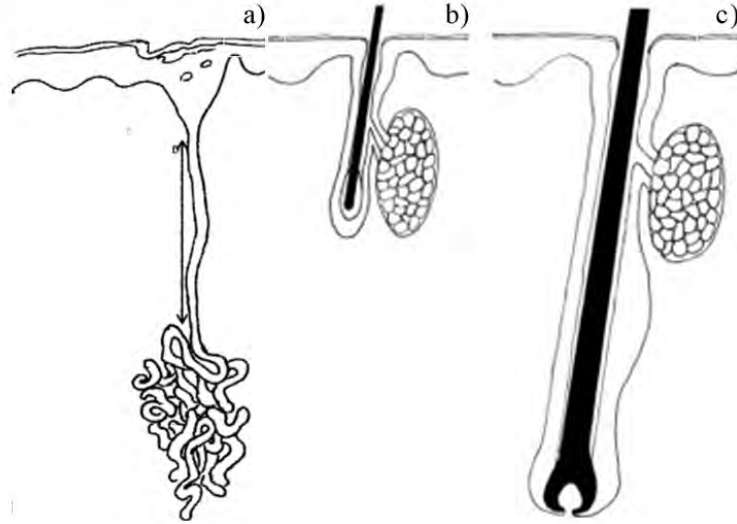


**Figure 1.2: Schematic of the skin non-linearities used as imperfections in this report,** with a) an eccrine sweat gland, b) a vellus hair follicle, and c) a terminal hair follicle. Note that the schematics are not on scale. Schematics retrieved from Wilke et al. (2007), and Hairless NYC Clinic (2014)

Eccrine sweat glands (from now on simply called sweat glands) are coiled tubular structures that already exist at birth and can be found all over the human body (Wilke et al., 2007). They are not to be confused with apocrine sweat glands, which are located around hair follicles (Wilke et al., 2007), and thus, cannot be used as separate skin non-linearities in the model.

Hairs are flexible strands of dead, keratinized cells largely produced by the hair follicles deep in the skin (Marieb and Hoehn, 2015). The two main components of the hair follicle are the root (where keratinization is still ongoing), and the shaft (where keratinization is completed) (Marieb and Hoehn, 2015). Due to stimulating effects of androgens (for example testosterone), hair can become coarser and longer on other places than the scalp. These visible hairs are called terminal hairs. Pale and fine (non-visible) hairs covering most of the human body are called vellus hairs.

All things considered, this report will try to answer the following research question:

*What are the effects of skin non-linearities, such as hair follicles or sweat glands, on excessive skin folding?*

It is hypothesized that the skin non-linearities at least trigger (or alter) the folding as explained earlier. This report will also examine the influence of multiple implemented skin non-linearities at once on the skin folding, to mimic the biological structure of the skin. No convincing literature has been found on the effect of multiple imperfections on the outcome of the folding process, nor on the effect of the imperfection depth. Thus, making it complicated to prescribe a well-argued hypothesis about these parameters.

In order to model excessive skin folding, a finite element model has been developed in the Abaqus/Explicit software (Abaqus/Explicit, 2021) (from now just called Abaqus), in support of a Python (Spyder Project Contributors, 2017; Van Rossum and Drake, 2009) script to implement the imperfections. This report has, as mentioned earlier, implemented the dermis and hypodermis layer

in a bi-layered structure with the simplifications aforementioned. As most biological tissues, the two layers show a non-linear stress/strain dependence, mainly due to re-organizing fibers (Oomens et al., 2017). Both the skin and fat layers were, thus, modelled according to the Neo-Hookean strain energy function. This accounts for non-linear mechanical behavior and large deformations (both occurring in excessive skin folding). Both properties are quite frequently ignored in papers (Oomens et al., 2017). At first in Chapter 2 the complete model setup will be elaborated, where first simple (only dermis) models, excluded from geometrical non-linearities, will be modelled in Abaqus and compared to the analytical solution of uniaxial compression and tension described in Oomens et al. (2018). Also, an adequate element size and time period for the simulation will be determined. The one layer dermis model then will be expanded to a bi-layered model of the skin, and subjected to sinusoidal folding based on a critical pressure  $p_{crit}$  described in (Budday et al., 2014). After the initial models are validated, geometrical non-linearities will be implemented into the model. Chapter 3 will show the folding results, where the data will be quantified by the normalized mean curvature  $\kappa^*$ , as described in (Wang et al., 2021). Chapter 4 will then discuss these results and its limitations before the report is concluded in Chapter 5.

# Chapter 2: Methods

In order to set up the most reliable and functional bi-layered skin model, the model had to be built from the ground up and subjected to several tests in order to validate the model's output. Initially in Section 2.1, methods to compose and test the benchmark model consisting of only the dermis skin layer are described. In Section 2.2, the methods used to expand the validated benchmark model with the implementation of the second layer, the hypodermis, will be explained. In Section 2.3, a description will be given on how the skin non-linearities were implemented as imperfections. And Section 2.4 will conclude the Methods chapter by describing the calculation of the normalized mean curvature  $\kappa^*$ , used to quantify the morphology of the final state.

Before diving into the process of building the model, it is convenient to address some of the settings used in Abaqus applicable for all the performed simulations in this report. In general, the model was constructed by using mostly the default settings in the software. Some choices, however, demand some elaboration. The pressure, for example, was decided to be applied to the structure via a smooth amplitude step as this prevented any (beforehand unexpected) fluctuations in potential energy curves. Secondly, an eight-node, continuum, hexahedral element type with reduced Gauss integration (C3D8R) was chosen. The reduced integration was chosen to decrease computational time, and to prevent volumetric locking phenomena in isochoric (or volume-invariant) materials (i.e. with a bulk modulus over shear modulus ratio of  $\gg 1$ ) (Doll et al., 1998).

## 2.1 The benchmark model

A model of only the dermis skin layer was processed in Abaqus as a benchmark model for any further adaptations. The benchmark model was subjected to several tests in order to validate the results of the simulations. First, the setup of the benchmark model consisting of just one element will be elaborated.

### 2.1.1 One-element model setup

A rather straightforward model of a one  $\text{m}^3$  cube, containing the dermis layer, was implemented in Abaqus. Mechanical properties of the dermis layer, mainly the Young's Modulus  $E = 0.066$  MPa, and the Poisson's ratio  $\nu = 0.49$ , were subtracted from (Shiihara et al., 2015). To model the non-linear mechanical behavior of the dermis, and to account for large deformations, the dermis was modelled according to the Neo-Hookean strain energy function as already mentioned in the Introduction (Chapter 1). The material parameters used in the Neo-Hookean formulation,  $C_{10}$  and  $D_1$ , were derived using

$$C_{10} = \frac{G}{2} \text{ and } D_1 = \frac{2}{K} \quad (2.1)$$

, where the shear modulus  $G$  and bulk modulus  $K$  are calculated using the earlier mentioned material properties  $E$  and  $\nu$ , namely by

$$G = \frac{E}{2(1+\nu)} \text{ and } K = \frac{E}{3(1-2\nu)} \quad (2.2)$$

The Poisson's ratio  $\nu$  was chosen to be nearly incompressible as Abaqus does not support a value of  $D_1$  equal to 0.

The cube of dermis material was fixed with symmetry boundary conditions (Figure 2.1) on the surfaces  $AEHD$ ,  $ABCD$ , and  $DCGH$  to maintain a free movement of the structure in all three dimensions. A pressure of 80 kPa (alternating either in tension or compression) was applied on the surface  $ABFE$ . The value of 80 kPa was chosen based on the analytical solution for incompressible Neo-Hookean solids that will be described and plotted in Section 2.1.2. According to this analytical solution, this value should reach stress ratios in x-direction of at least  $\lambda_x \in [0.5, 2]$ , which corresponds to large displacements seen in excessive skin folding. To check for time independency, the total time period of the simulation alternated between 1, 10 and 100 seconds.

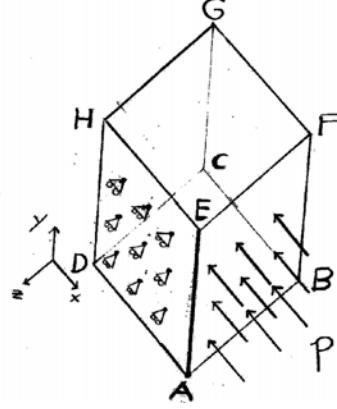


Figure 2.1: Sketch of the boundary conditions in the benchmark model of the dermis.

### 2.1.2 Analytical solution of the one-element benchmark model.

Before enhancing the one-element model applied in Section 2.1.1 with the addition of multiple elements, and the additional tissue layer, the one-element model was first validated with an analytical solution using the constitutive equation for incompressible Neo-Hookean solids

$$\boldsymbol{\sigma} = K(J - 1)\mathbf{I} + \frac{G}{J}\tilde{\mathbf{B}}^d \quad (2.3)$$

found in (Oomens et al., 2018). With no shear stresses involved in the analytical solution and assuming homogeneous deformation, the deformation tensor ( $\mathbf{F}$ ) can be described with stretch ratios  $\lambda_i$  as follows

$$\mathbf{F} = \lambda_x \vec{e}_x \vec{e}_x + \lambda_y \vec{e}_y \vec{e}_y + \lambda_z \vec{e}_z \vec{e}_z \quad (2.4)$$

The volume ratio  $J$  can be calculated with

$$J = \det(\mathbf{F}) = \lambda_x \lambda_y \lambda_z \quad (2.5)$$

The deviatoric part of the isochore left Cauchy-Green tensor  $\tilde{\mathbf{B}}$  is defined by

$$\tilde{\mathbf{B}}^d = \tilde{\mathbf{B}} - \frac{1}{3} \text{tr}(\tilde{\mathbf{B}})\mathbf{I} = J^{-\frac{2}{3}} \mathbf{F}\mathbf{F}^T - \frac{1}{3} \text{tr}(J^{-\frac{2}{3}} \mathbf{F}\mathbf{F}^T)\mathbf{I} \quad (2.6)$$

, and can be calculated by substituting Equations 2.4 and 2.5 into Equation 2.6. Substituting the calculated  $\tilde{\mathbf{B}}^d$  in Equation 2.3 provides an analytical solution for the Cauchy stress tensor  $\boldsymbol{\sigma}$ . The normal components of  $\boldsymbol{\sigma}$  are given by

$$\sigma_{xx} = K(J - 1) + \frac{GJ^{-\frac{5}{3}}}{3}(2\lambda_x^2 - \lambda_y^2 - \lambda_z^2) \quad (2.7)$$

$$\sigma_{yy} = K(J - 1) + \frac{GJ^{-\frac{5}{3}}}{3}(-\lambda_x^2 + 2\lambda_y^2 - \lambda_z^2) \quad (2.8)$$

$$\sigma_{zz} = K(J - 1) + \frac{GJ^{-\frac{5}{3}}}{3}(-\lambda_x^2 - \lambda_y^2 + 2\lambda_z^2) \quad (2.9)$$

The skin layer is free to move in y- and z-direction, meaning  $\sigma_{yy} = \sigma_{zz} = 0$ , and consequently

$$K(J - 1) = -\frac{GJ^{-\frac{5}{3}}}{3}(-\lambda_x^2 + 2\lambda_y^2 - \lambda_z^2) = -\frac{GJ^{-\frac{5}{3}}}{3}(-\lambda_x^2 + 2\lambda_y^2 - \lambda_z^2) \quad (2.10)$$

Substituting  $K(J - 1)$  from Equation 2.10 in Equation 2.7 gives

$$\sigma_{xx} = GJ^{-\frac{5}{3}}(\lambda_x^2 - \lambda_y^2) \quad (2.11)$$

By using Equation 2.2 and Equation 2.5, under the assumption of incompressibility  $J = 1$ , leads to the final analytical expression

$$\sigma_{xx} = \frac{E}{2(1 + \nu)}\left(\lambda_x^2 - \frac{1}{\lambda_x}\right) \quad (2.12)$$

Results of the one-element benchmark model can be seen in Figure 2.2.

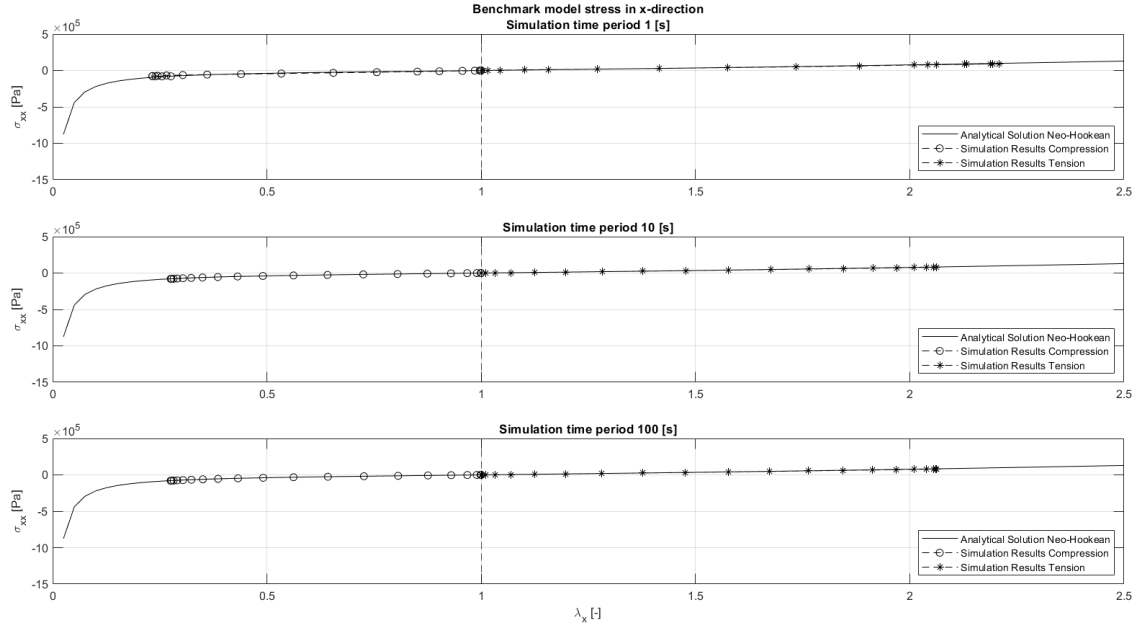


**Figure 2.2: Stress over stretch results for the dermis skin layer under either compression, or tension.** The analytical derived solution follows the constitutive equation for an incompressible Neo-Hookean solid. The simulation results are from the one-element benchmark model, modelled in Abaqus.

From Figure 2.2 it becomes clear that all simulations agree with the analytical solution. Furthermore, the simulation is time independent, one of the requirements for a quasi-static simulation besides the minimum contribution of inertial forces to the system. The threshold of minimum inertial effects in the system has been set to a maximum of 5% of kinetic energy compared to internal energy in the system, as depicted by Abaqus/Explicit (2021). The energies in the different simulations (compared only for the compression simulations) can be found in Figure 2.3. The figure indicates that the longer the simulation time, the more quasi-static the analysis becomes. Both potential energy and kinetic energy values early in the simulation are negligibly small, meaning that the 10 and 100 seconds simulations are quasi-static.

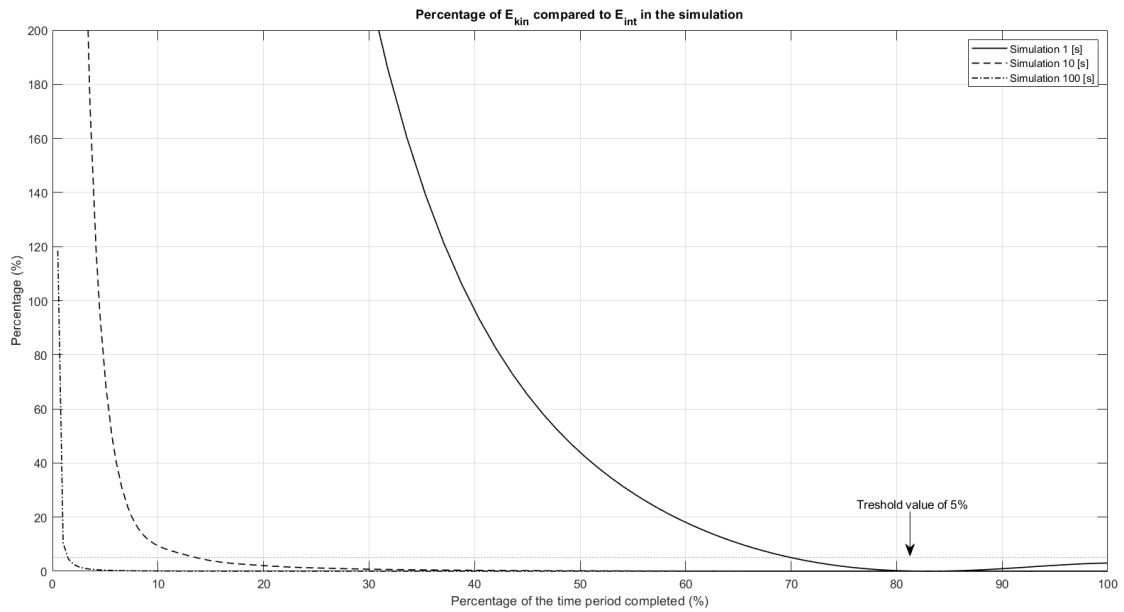


**Figure 2.3: Energetic state of the simulation over the percentage of time up until completion of the simulation.** For the one-element compression simulations, the percentage of kinetic energy  $E_{kin}$  over the internal energy  $E_{int}$  have been plotted for different time periods simulated.

### 2.1.3 Multiple element benchmark model

The initial one-element simulation in Section 2.1.1 and 2.1.2 validated the model's outcome with the theoretical values from the constitutive equation of incompressible Neo-Hookean solids. It also gave an indication about a possible time period to be used in order obtain a quasi-static analysis. It was chosen to estimate the correct time period by analyzing multiple possibilities and evaluate them for realistic results and quasi-static energy distributions.

First of all, the one-element model of the dermis skin layer from Section 2.1.1 was expanded with finer meshes of the cube containing either 125, 1000 or 8000 elements. These correspond to mesh sizes of 0.2, 0.1, and 0.05 m. To further examine for the best time period, all three possible meshes were subjected to simulations with time periods of either 5, 10, 15, 100 or 1000 seconds. The same pressure of 80 kPa was applied on surface  $ABFE$  (Figure 2.1). In addition to the model in Section 2.1.1, both surfaces with normal in either positive or negative z-direction (surfaces  $AEHD$  and  $BFGC$ ) were fixed with symmetry boundary conditions, to already mimic the continuous structure of the abdomen skin. Furthermore, the 1 second simulation was already considered not quasi-static (and thus inadequate) following the results in Figure 2.3. A same conclusion could be drawn for an 8000 element model after just a short time of simulating, as all of these simulations failed due to excessive distortions of the elements. This was probably due to numerical instabilities (Abaqus/Explicit, 2021). For the same reason, simulations with a time period of 1000 seconds or more were inadequate as well.

Multiple field outputs were collected for both the 125 and 1000 elements simulations. These field outputs consisted of the Von Mises stress ( $\sigma_{VM}$ ), normal stress components ( $\sigma_{xx}$ ,  $\sigma_{yy}$  and  $\sigma_{zz}$ ) and one shear stress component ( $\sigma_{xy}$ ). From these field outputs, the Von Mises stress comparison is displayed in Figure A.1 in Appendix A.1 as an example. All the field outputs indicated that the variations in the simulation results between the different number of used elements seem negligible. However, the solutions are not entirely time independent as especially the simulations performed with a time period of 5 and 100 seconds deviate slightly, but noticeably from the 10 and 15 seconds simulations. Assuming the simulation with the most elements and longest time period (i.e. 1000 elements and 100 seconds) is the most precise, additional simulations with time periods of 25, 50, 75, 125 and 150 seconds (and 1000 elements) were performed to, eventually, use the most accurate,

but also least costly model before implementing the second tissue layer. Results of this second Von Mises stress comparison can be seen in Figure 2.4.

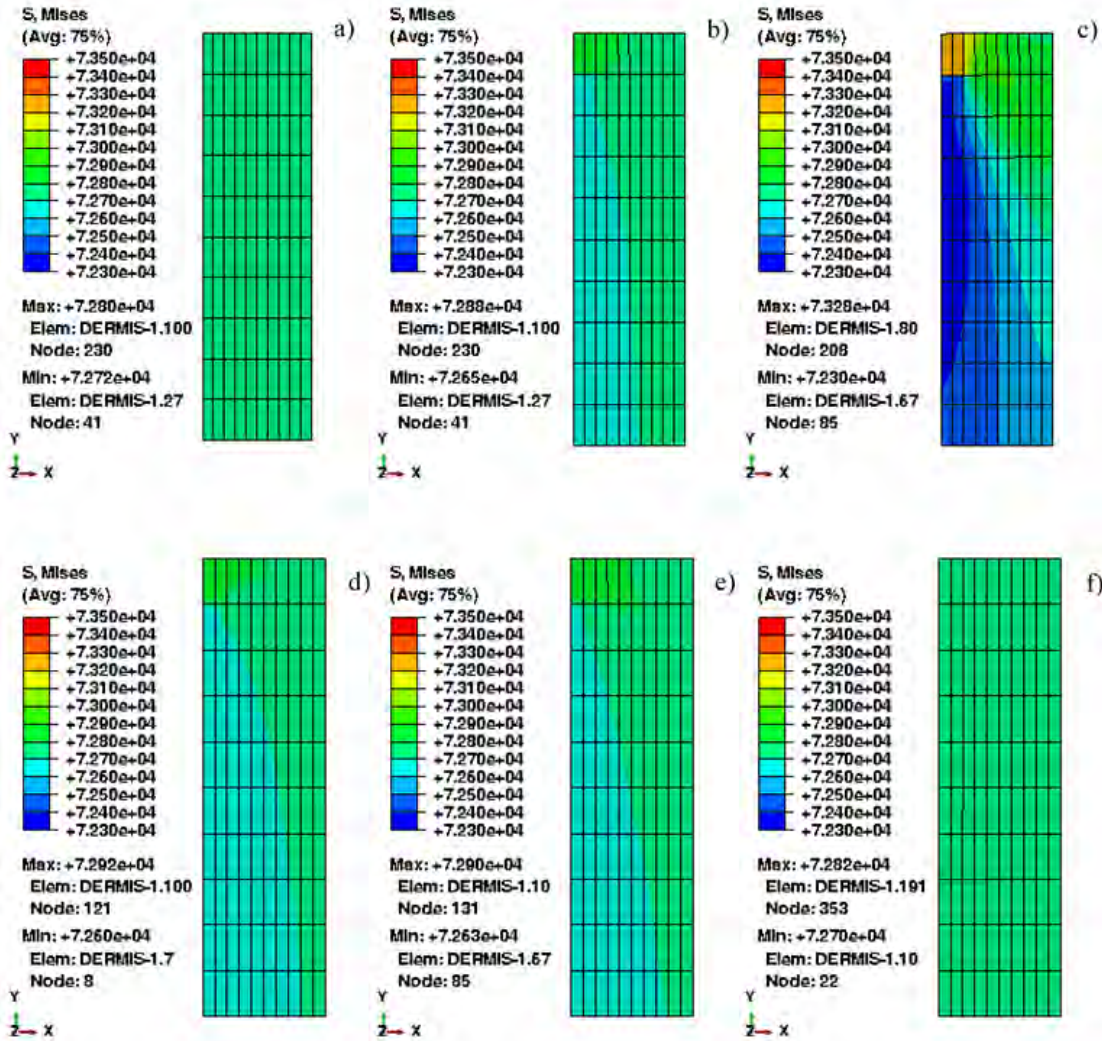


Figure 2.4: Results of the Von Mises stress analysis of the benchmark model simulations with 1000 elements. Time periods consist of a) 25, b) 50, c) 75, d) 100, e) 125 and f) 150 seconds.

Apart from the 75 seconds simulation, the benchmark solution seems time independent at time periods above 25 seconds. The strange behavior at a time period of 75 seconds cannot be explained, and was visible for an extra test simulation of 80 seconds as well. Nevertheless, the results in Figure 2.4, and an additional check for the irrelevance of inertial forces to ensure a quasi-static analysis proved that a simulation of 1000 elements during a time period of 50 seconds was the best balance between a reliable outcome and minimum computational cost. These values can be used for the simulations of the bi-layered model of the skin.

## 2.2 Bi-layered, multiple element model of the dermis and hypodermis.

The final model in Section 2.2 was expanded with the hypodermis layer. The hypodermis was also modelled based on the Neo-Hookean strain energy function. Similar to the dermis layer, the hypodermis was assumed to be nearly incompressible ( $\nu = 0.49$ ), but, to have a Young's Modulus of 0.0066 MPa (Shihara et al., 2015). The one m<sup>3</sup> cube was partitioned in Abaqus in a one over nine ratio, where the dermis layer was the thinnest layer. Although this ratio does not agree with biological skin dimensions, it does agree with an analytical solution for bi-layered sinusoidal folding on an assumed infinite large elastic substrate (Budday et al., 2014). This analytical solution is used as a template for modeling the folding process in this report. It predicts the critical pressure,  $p_{crit}^{ana}$  for folding to occur (Equation 2.13), and the waveform of this folding  $\lambda_{crit}^{ana}$  (Equation 2.14)

$$p_{crit}^{ana} = \frac{3}{4} \frac{E_{HD}}{1 - \nu_{HD}^2} \sqrt[3]{\frac{1}{3} \frac{1 - \nu_{HD}^2}{1 - \nu_D^2} \frac{E_D}{E_{HD}}} \quad (2.13)$$

$$\lambda_{crit}^{ana} = 2\pi t_D \sqrt[3]{\frac{1}{3} \frac{1 - \nu_{HD}^2}{1 - \nu_D^2} \frac{E_D}{E_{HD}}} \quad (2.14)$$

, with subscripts  $D$  and  $HD$  standing for dermis and hypodermis respectively, and  $t_D$  being the thickness of the dermis.

In one of the earlier simulations presented in Appendix A.2, it was concluded that the folding of the model is mesh independent for different mesh sizes in the dermis and hypodermis layer. It was thus decided to adapt the 1000 element model from Section 2.1.3 in model with a denser mesh on the dermis layer (element size of 0.033 m), and a less dense mesh in the hypodermis layer (vertical mesh size of 0.18 m and horizontal mesh size of 0.033 m).

The bi-layered model made use of an Abaqus coupling constraint on the pressurized surface  $ABFE$  (Figure 2.1) Due to this coupling constraint, a concentrated force  $F_C = -8$  kN had to be applied on this surface instead of a pressure used earlier. This value for the concentrated force resulted in simulations that included the start of the folding, and the final state of the folding without causing excessive distortions.

Another difference of the finalized model compared to the benchmark model in Section 2.1.3 were the dimensions, as it was decided to expand the model in x-direction to trigger the sinusoidal folding. The model dimensions were set to a two by one by one m<sup>3</sup> beam. Although not entirely representative to the skin dimensions in a human being, it was decided to stay in this meter scale to make sure the simulation remained quasi-static and stable as conducted in earlier tests. Still, a simulation in realistic human skin dimensions of several millimeters, without imperfection, was conducted as well and checked for similar results seen in the meter scale model. The results of this check can be seen in Appendix A.3. Von Misses stress states of both simulations were similar, however, there was a difference in top surface morphology of the final states. Nevertheless, it was concluded that the meter scale model remained the most favorable one simply due to the lower computational costs, and due to stability concerns in the millimeter scale model. Results of the first folding simulation can be seen in Figure 2.5. Furthermore, Figure 2.6 was used to validate the Abaqus model with the analytical solution for sinusoidal folding in Budday et al. (2014).

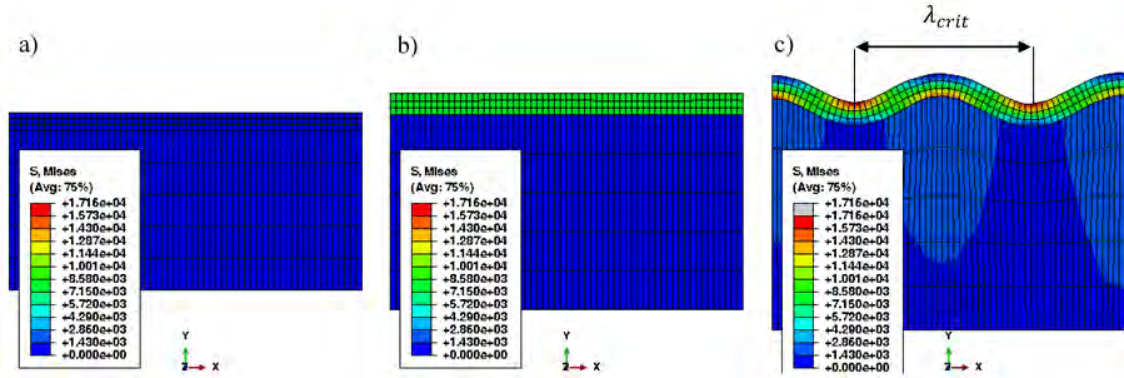


Figure 2.5: Von Mises stress results of the sinusoidal folding simulation Where a) is the initial situation, b) the last frame before folding occurs, and c) the first frame with visible folding.

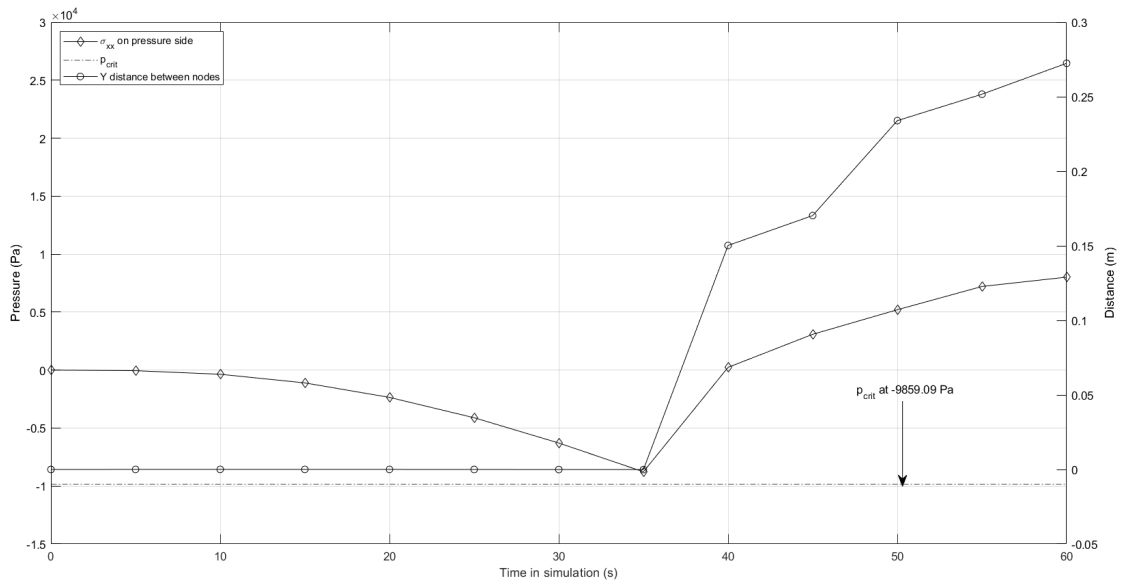


Figure 2.6: Normal stress component  $\sigma_{xx}$  in the dermis layer and y-distance between a node on the top of the folding and a node on the bottom of the folding. Both plotted against the simulation time.

In Figure 2.6, it can be seen that a distance in nodal y-coordinates other than 0 (used as folding indicator) occurs only after the normal stress  $\sigma_{xx}$  in the dermis layer has reached a value of (approximately)  $p_{crit}^{sim} = -8000$  Pa. This value approximates the analytical  $p_{crit}^{ana} = -9860$  Pa value. The same holds for the simulated critical wavelength  $\lambda_{crit}^{sim}$ , which was directly determined in Abaqus to be 0.85 m. Again, closely approximating the analytical  $\lambda_{crit}^{ana}$  of 0.94 m. Following these results, it was decided to continue with implementing the skin non-linearities.

### 2.3 Implementation of skin non-linearities.

The skin non-linearities were implemented as nodal displacements (also known as imperfections) into the Abaqus keyword section of the finalized bi-layered model in Section 2.2. For the non-linearities, three distinct types were used mainly sweat glands, vellus (non-visible) hair follicles, and terminal (visible) hair follicles, already shown and explained in the Introduction (Chapter 1).

Approximate values for the thickness (noted as the diameter of the imperfection on the top surface of the skin), depth, and distribution of these skin non-linearities can be found in Table 2.1.

**Table 2.1: Literature data corresponding to skin non-linearities implemented in the Abaqus model.**

Non-linearity type	Distribution (nr./cm <sup>-2</sup> ) <sup>a</sup>	Depth ( $\mu m$ )	Diameter ( $\mu m$ )
Sweat glands	$190 \pm 5$	$2432 \pm NaN$ <sup>b,c</sup>	$100 \pm NaN$ <sup>d</sup>
Vellus hairs	$70 \pm 15$ <sup>e</sup>	$646 \pm 140$ <sup>f</sup>	$30 \pm NaN$ <sup>f</sup>
Terminal hairs	$70 \pm 15$ <sup>e</sup>	$4864 \pm 605$ <sup>f</sup>	$100 \pm NaN$ <sup>f</sup>

<sup>a</sup>(Szabo, 1967)

<sup>b</sup>Paper only mentions them to be approximately half of a terminal hair

<sup>c</sup>(Takagi and Tobaru, 1954)

<sup>d</sup>(Wilke et al., 2007)

<sup>e</sup>Paper made no distinction between vellus and terminal hair distribution, but counted them both.

<sup>f</sup>(Wosicka and Cal, 2010)

In total, twelve simulations were performed consisting of:

1. One control simulation without imperfections.
2. Three simulations with both one imperfection on a fixed node (somewhere in the middle) on the top surface of the skin model. The simulations differ in the type of skin non-linearity implemented.
3. Three simulations with an average number of imperfections corresponding to a particular skin non-linearity. Number of imperfections were determined based on the "Distribution" values in Table 2.1, which will be elaborated further in Section 2.3.2.
4. Five simulations under a constant, average number of sweat glands imperfections, but, varying hair imperfections in both number and type (either vellus or terminal). Further elaborations can be found in Section 2.3.3.

The next subsections will elaborate on the implementation of the imperfections in the different models.

### 2.3.1 Method of implementing the imperfection

The imperfections were only implemented in the dermis layer of the model which consists of three elements in height. To distinct between the different skin non-linearities, the depth of the imperfection was scaled according to the biological values for skin non-linearity depth in Table 2.1. A biological reference depth of the dermis layer of 5 mm was considered and used to calculate the fraction of the dermis which the skin non-linearity penetrates. This fraction was then used to find the needed nodal y-displacement for the imperfection in the model, where the dermis had a height of 0.1 m. This meant a nodal y-displacement for the top surface node of  $-0.039$ ,  $-0.013$ , and  $-0.077$  m in the model for respectively the sweat gland, vellus hair, and terminal hair imperfection. To ensure this node stays on the top surface and does not cross any other nodes, the underlying three nodes had to be displaced as well. By ignoring any displacement of the bottom node that intersects with the hypodermis layer, displacements of the intermediate nodes could easily be deduced using the top nodal y-displacement. For this it was important to preserve an equal distance between (in y-direction) adjacent nodes. Writing the imperfection output in the model definition in Abaqus was done automatically via a Python script.

### 2.3.2 Determining the number of imperfection nodes

For the eight simulations using the distribution values in Table 2.1, multiple imperfections had to be implemented at ones. The method for implementing the imperfections was the same method as prescribed in Section 2.3.1. However, the number of nodes corresponding to a skin non-linearity had yet to be determined. The number of skin non-linearities (per type) ( $N_i$ ) on a two m<sup>2</sup> skin surface ( $A_{tot}$ ) was simply derived from the distribution values in Table 2.1. However, the mesh density of the dermis layer proved to be a problem as it is impossible to use a mesh density capable of implementing  $N_i$  (in  $\mathcal{O}(10^5) - \mathcal{O}(10^6)$ ) imperfections. Thus, an adequate fraction to translate the number of non-linearities into the number of nodes ( $n_i$ ) relative to the total number of nodes on the top surface ( $n_{tot}$ ), was determined with

$$n_i = f * n_{tot} \quad (2.15)$$

, and

$$f = \frac{A_i}{A_{tot}} = \frac{N_i}{2} \pi \left(\frac{d_i}{2}\right)^2 = \frac{N_i \pi d_i^2}{8} \quad (2.16)$$

With  $N_i$  the number of skin non-linearities of type  $i$  determined earlier,  $A_i$  the total surface of the  $N_i$  non-linearities and,  $d_i$  the diameter of the skin non-linearity  $i$  (in m) noted in Table 2.1. All these calculations were implemented in the same Python script mentioned earlier, as well as the random placement of these  $n_i$  nodes on the top surface of the model.

No further adaptations were necessary for the sweat gland imperfections, however, an extra adaptation to the method was necessary for the vellus hairs and terminal hairs in the model. An elaboration of this adaptation will be provided in the next section.

### 2.3.3 Terminal hair count using the Ferriman & Gallwey score

It may be clear that a human being, with uncountable number of hairs on its body, cannot solely consist of terminal hairs. This fact was also considered in the model by using the Ferriman and Gallwey method (short, FG method), initially used for hirsutism diagnosis on females (Ferriman and Gallwey, 1961). The FG method is a subjective method to classify the severity of terminal hair growth on (potential) hirsutism patients. The FG method uses a score from 0 – 4 with a score of 0 corresponding to no evident terminal hair, up till a score of 4 corresponding with extensive terminal hair growth, generally seen in males (Yildiz et al., 2009). Unfortunately, no distributions of terminal hairs were mentioned per FG grade in (Ferriman and Gallwey, 1961) or (Yildiz et al., 2009). Thus, an estimation had been made on the percentage of hair non-linearities to be terminal hairs, per FG grade. This estimation can be seen in Table 2.2.

**Table 2.2: Percentage of nodal hair imperfections to behave as a terminal hair. Based on the Ferriman & Gallwey score.**

FG grade	Percentage of $n_{hair}$ (%)
FG0	0
FG1	5
FG2	12.5
FG3	25
FG4	40

## 2.4 Quantifying the results: normalized mean curvature $\kappa^*$

To quantify the folding results, a 3D curvature calculation method described in (Wang et al., 2021) was used. Firstly, the initial coordinates  $(x_0, y_0, z_0)$  and final coordinates  $(x, y, z)$  of the integration points (one per element, due to reduced integration) were retrieved from the Abaqus output using a Python script. The data following the Python script was then post-processed in MATLAB (MATLAB, 2021). For every integration point, the eight (if possible) adjacent integration points in the initial state were selected and their corresponding final coordinates were fitted to a plane using the *polyfitn* toolbox in MATLAB (D'Errico, 2021). The fitted plane was of the polynomial form

$$y = ax + bz + c \quad (2.17)$$

The components of the outward normal vector of these planes were determined by

$$n_x = \frac{-a}{\sqrt{a^2 + b^2 + 1}} \quad n_z = \frac{-b}{\sqrt{a^2 + b^2 + 1}} \quad n_y = \frac{1}{\sqrt{a^2 + b^2 + 1}} \quad (2.18)$$

, while considering the Cartesian coordinate system used in Abaqus and displayed in Figure 2.1. The calculated normal vector was used to define a local coordinate system around the eight adjacent integration points, and eventually used to fit a paraboloid through the eight integration point plus the integration point under evaluation. To translate the normal in a local coordinate system, matrix

$$\mathbf{Q} = \begin{bmatrix} \frac{n_x^2 n_y + n_z^2}{n_x^2 + n_z^2} & \frac{-n_x n_z (1 - n_y)}{n_x^2 + n_z^2} & -n_x \\ \frac{-n_x n_z (1 - n_y)}{n_x^2 + n_z^2} & \frac{n_x^2 + n_z^2 n_y}{n_x^2 + n_z^2} & -n_z \\ n_x & n_z & n_y \end{bmatrix} \quad (2.19)$$

was used in

$$\begin{bmatrix} x'_i \\ z'_i \\ y'_i \end{bmatrix} = \mathbf{Q} \begin{bmatrix} x_i - x_9 \\ z_i - z_9 \\ y_i - y_9 \end{bmatrix} \quad (2.20)$$

to calculate the final deformed coordinates (in the local coordinate system) of the eight adjacent integration points  $i$ . The coordinates  $x_9$ ,  $z_9$ , and  $y_9$  correspond to the deformed Cartesian coordinates of the evaluated integration point.

In the local coordinate system, a paraboloid

$$y'_i = \alpha x_i'^2 + \beta z_i'^2 + \gamma x_i' z_i' \quad (2.21)$$

was fitted which lead to eight equations with three unknowns  $(\alpha, \beta, \gamma)$ . The parameters (stored in a three by one array  $[d]^T$ ) can be calculated by

$$[d]^T = ([A]^T [A])^{-1} [A]^T [z]^T \quad (2.22)$$

With  $[A]$  an eight by three matrix containing the values  $(x_i'^2, z_i'^2, x_i' z_i')$ , and  $[z]^T$  the eight measurements of  $z'_i$  in a eight by one array. By definition, the mean curvature  $\kappa$  was determined by

$$\kappa = \frac{-1}{2} \left( \frac{\partial^2 z'}{\partial x'^2} + \frac{\partial^2 z'}{\partial y'^2} \right) = -(\alpha + \beta) \quad (2.23)$$

, which was derived from Equation 2.21. Finally, the mean curvature is normalized to obtain the normalized mean curvature

$$\kappa^* = \kappa t_D \quad (2.24)$$

, where  $t_D$  is the initial thickness of the dermis. An example of how the curvature algorithm was validated can be found in Appendix A.4.

# Chapter 3: Results

In this chapter the results of the final bi-layered model simulations, as concluded in Section 2.2, and possibly extended with imperfections as described in Section 2.3, will be presented. The results will be presented in the same order as noted in Section 2.3, starting with the results of the control group and the one imperfection simulations.

## 3.1 Control group & one imperfection simulations

In post-processing the results of the control group and the one imperfection simulations, first the different states of the model were analyzed using the plots automatically provided by Abaqus and shown in Figure 3.1. The first thing to note is some distortion in the first folding frame of the terminal hair imperfection, probably caused by the relatively large displacement of the imperfection related to this skin non-linearity. Furthermore, it can be distinguished that the control group differs in final top surface morphology compared to the one imperfection simulations, in that the control group has no typical fold in the middle of the structure. When comparing the one imperfection simulations with each other, more or less the same results are visible as a clear fold occurs somewhere in the middle of the structure. The Von Mises stress states shown in Figure 3.1 show similar behavior in all simulations.

The one imperfection simulations were analyzed more in detail by examining the time of folding to start (Figure 3.2), and the normalized mean curvature  $\kappa^*$  of these simulations (Figure 3.3). In Figure 3.2 similar results for the one imperfection simulations can be seen as in Figure 2.6 for the control simulation. For all the one imperfection simulations, the folding starts at a normal stress  $\sigma_{xx}$  on the dermis layer of approximately  $p_{crit}^{sim} = -8000$  Pa, and at a simulation time of approximately 35 seconds.

Evaluating  $\kappa^*$  in Figure 3.3, the vellus hair imperfection and the sweat gland imperfection follow a parallel trend with a negative normalized mean curvature  $\kappa^*$  on the location of the fold that reaches an approximate extreme value of  $-2.4$ . The terminal hair imperfection shows slightly different behavior concerning the normalized mean curvature  $\kappa^*$  as the fold itself is moved backwards a bit compared to the other skin non-linearities, and that it reaches a higher extreme value of  $\kappa^* = -3.1$ .



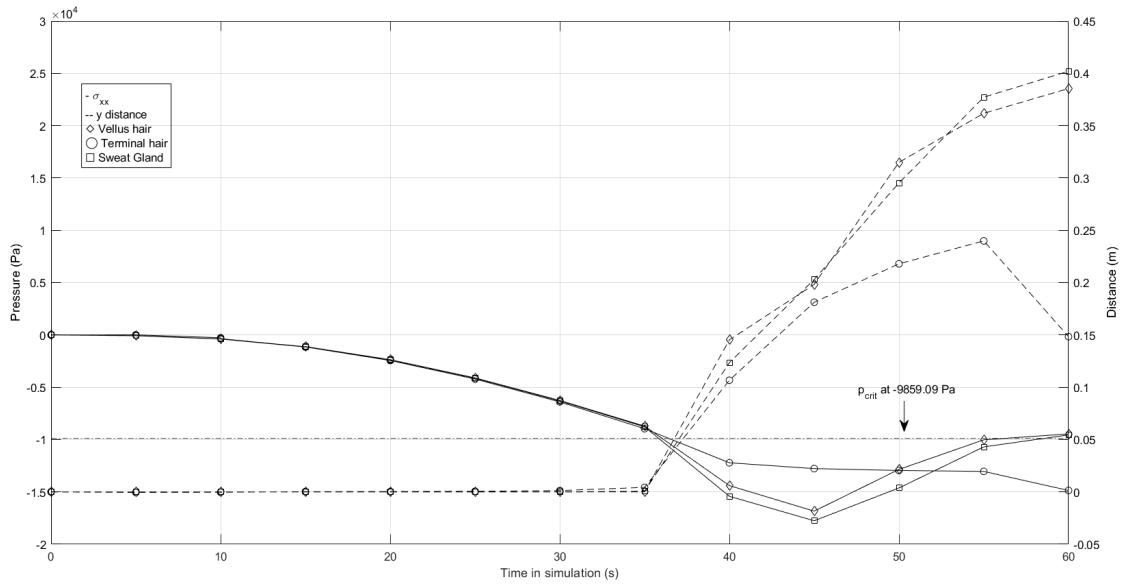


**Figure 3.2:** Normal stress component  $\sigma_{xx}$  on the dermis layer, and y-distance between a node on the top of the folding and a node on the bottom of the folding. Both plotted against the simulation time. Results of the one imperfection simulations are shown.

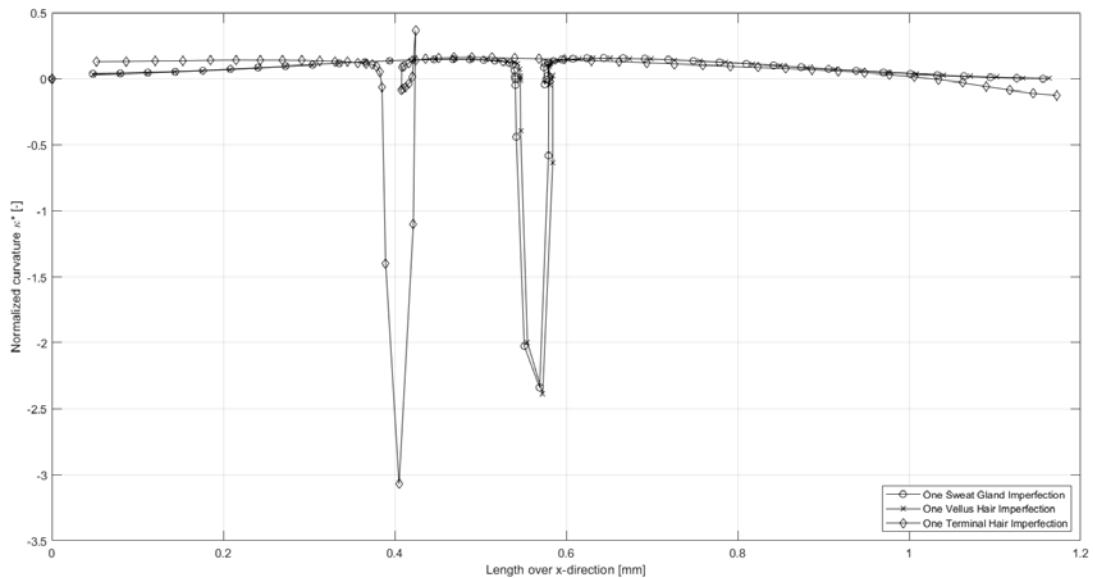


**Figure 3.3:** Normalized mean curvature  $\kappa^*$  of the one imperfection simulations plotted over a line in the middle of the model. Results shown from final state of the model.

### 3.2 Mean distribution of skin non-linearities simulations

Similar to the previous Section 3.1, first the initial Abaqus output was examined for the mean distribution of imperfections for the different skin non-linearities. These results are displayed in Figure 3.4.

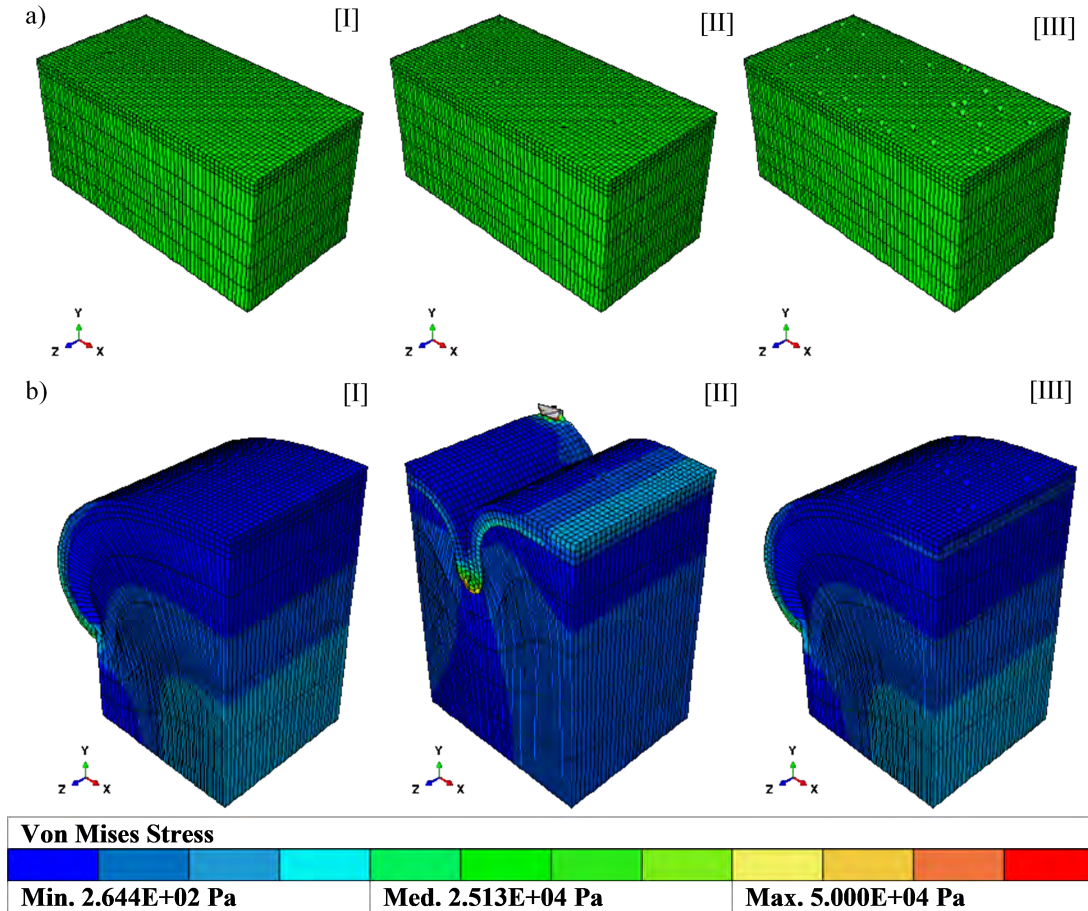


**Figure 3.4: Von Mises stress displayed in two states of the simulation with average distributed imperfections.** The rows show the state of the model with a) being the initial state, and b) the final state. The columns [I], [II], and [III] stand for the mean FG0 distribution of hair, mean FG4 distribution of hair, and mean distribution of sweat glands respectively. Further note that a grey scaled color in the figure represents a stress higher than shown in the colored label

Again, it has to be noted that an element is distorted, this time in the final state of the simulation with hair distributed with grade FG4. The distortion is probably caused by the placement of the imperfection close to the edge of the model. Also, for the same simulation, the results are similar to the one imperfection simulations in Section 3.1. The hair distributed with grade FG0 and the sweat gland distribution both show a new morphology in the final state with a fold occurring at the backside of the structure.

Furthermore, the start of the folding procedure (and under which normal pressure  $\sigma_{xx}$  on the dermis layer), and the normalized mean curvature  $\kappa^*$  of the simulations were examined in similar ways as displayed in Figure 3.2, and Figure 3.3. Again (sinusoidal) folding starts at a time period of 35 seconds when a normal stress  $\sigma_{xx}$  of approximately  $p_{crit}^{sim}$  has been reached (for all

mean distributed simulations). Following Figure 3.4, it has already become clear that the mean curvature would differ between the different displayed simulations. The simulations with backside folding (i.e. with mean sweat gland and mean FG0 hair distribution) show  $\kappa^* \in (-0.5, 0.5)$ , with both negative and positive curvatures at the location of the folding. The simulation with a folding in the middle (e.g. the FG4 hair distribution) shows a similar pattern as shown for the one terminal hair imperfection in Figure 3.3, with also an extreme value of approximately  $-3.1$  for  $\kappa^*$ . Due to the similarities of the results, both plots are not shown.

### 3.3 Varying Ferriman & Gallwey score simulations

The final state of the results with different quantities of terminal hairs based on the Ferriman Gallwey scale described in Table 2.2 (combined with the mean sweat gland distribution) showed two final morphologies: 1) a sharp, folding occurring in the middle of the structure similar to Figure 3.1 column [III] and Figure 3.4 column [II] (applicable for the simulation with FG1 score), and 2) a folding at the backside of the structure similar to the folding in Figure 3.4 column [I] and [III] (applicable for the simulations with FG0, FG2, FG3 and FG4 score). All the different hair quantities simulations also started the (sinusoidal) folding at the exact same time in the simulation (around 35 seconds), and after the same normal stress  $\sigma_{xx}$  on the dermis layer was reached (around  $p_{crit}^{sim}$ ). The normalized mean curvature patterns showed similar results as seen in previous sections. For the FG1 score simulations that means a sharp downwards peak at the site of the folding, again similar to the one imperfection simulations in Figure 3.3. The extreme value for  $\kappa^*$  is a bit higher though and is about  $-5.7$ . For the remaining simulations in this section it holds that  $\kappa^*$  can be found in the region  $\kappa^* \in (-0.5, 0.5)$ , similar to the results in Section 3.2.

# Chapter 4: Discussion

Excessive skin folding after heavy weight loss becomes more and more of an issue as post bariatric surgery patients require additional contouring surgery to obtain the most satisfying results (Song et al., 2006; Toma et al., 2018). In order to minimize surgical intervention in obesity patients, it could be useful to, patient specific, predict the possibility of excessive skin folding before performing bariatric surgery. An interest is taken in the effect of so-called skin non-linearities, like hair follicles or sweat glands, on the excessive skin folding process. In cortical folding examples (Garcia et al., 2018; Wang et al., 2021) non-linearities are implemented in finite element models as imperfections. As a result, the imperfections trigger the folding, either by starting the folding procedure, or by changing the final state morphology of the folding (Garcia et al., 2018). In both cases, the imperfections lower the potential energy of the system (Mavrodontis, 2017). The interested skin non-linearities can be implemented as imperfections of a finite element model as well. The effects of multiple imperfections, or varying depths of imperfections on the folding, have not been researched yet, but are of particular interest for the excessive skin folding.

Results in Figure 3.1 of this report show that any imperfection, regardless of the depth, can alternate the position (and thus morphology) of the folding compared to the control simulation without any imperfection. This confirms the hypothesis that the skin non-linearities can trigger the excessive skin folding outcome. Varying depths of the imperfections can have an influence on the normalized mean curvature  $\kappa^*$  (or sharpness) of the folding as the deepest imperfection (a terminal, visible hair going approximately 97% deep into the skin) shows an extreme value of approximately  $\kappa^* = -3.1$ , as can be seen in Figure 3.3. In comparison, an extreme value of approximately  $\kappa^* = -2.4$  can be seen for the simulations with a vellus, non-visible hair, and a sweat gland imperfection. This result, however, argues the effect of imperfection depth on the folding as the vellus hair follicle imperfections penetrate the dermis layer less deep than the sweat gland imperfections (13% over 49% in). The difference seen between the terminal hair imperfection and the other groups is, thus, not validated. A last thing to note concerning the imperfection depth is that, for simplicity of the model, a rather large biological reference depth for the dermis of 5 mm was chosen to fit all the imperfections in the dermis layer. From literature, however, it is known that a typical dermis layer in the abdomen skin can be 2 to 4 mm in depth (Jain et al., 2013), and that terminal hair follicles can easily penetrate the hypodermis (Wosicka and Cal, 2010). It is recommended to model this penetration of the hypodermis by terminal hairs in further research as no imperfection was placed in the second layer of the model in this report. Another recommendation for further research, considering the imperfections, is to implement the thickness of the varying imperfections into the model. A terminal hair follicle disturbs the structures linearity more than a vellus hair follicle as it is not only larger in depth, but also in thickness inside the skin's structure. More nodes on the top surface, or more displacements in different directions than only nodal y-displacement might have to be implemented into the model to mimic the thickness of the skin non-linearities.

From the results in Section 3.1 it is, furthermore, noteworthy to mention that the imperfections have no influence on the critical pressure  $p_{crit}^{sim}$  for the first folding to occur. A similar trend has been described in the text of Section 3.2 and Section 3.3 where multiple imperfections per simulation were implemented. The start of the folding, thus, is not dependent on the skin non-linearities in the structure. To resume with the results in Section 3.2, where multiple imperfections of one kind were implemented into the structure, a new type of folding, where the folding occurs on the

back of the structure, emerged as can be seen in Figure 3.4. This new type of folding occurred for the mean distribution of vellus hair follicles, and sweat glands on the structure (based on distribution values mentioned in (Szabo, 1967) and processed in Section 2.3.2). A type of folding shown earlier in the simulations with a single implemented imperfection (see Figure 3.1), namely with a folding occurring in the middle of the structure, is also visible for the mean distribution of FG4 score hair imperfections (combined vellus and terminal hair imperfections, details on the Ferriman and Gallwey scale in Section 2.3.3). The mean curvature of this folding shows the same value of  $\kappa^* = -3.1$  as seen in the single terminal hair imperfection simulation earlier. Curvature of the backside foldings show lower values in the range of  $\kappa^* \in (-0.5, 0.5)$ , probably due to a lack of self-contact of the surface on the backside of the structure. It is interesting to discuss why this type of folding on the backside occurs. For the mean sweat gland distribution in Figure 3.4(a.III), no clear explanation can be given on why the model reaches the lowest energy state via this folding. Coincidence happens, however, that the mean FG0 distribution (only vellus hair) in Figure 3.4(a.I) consists of mere one imperfection randomly placed on the structure (as derived using the algorithm described in Section 2.3.2). This makes it possible to compare Figure 3.4(b.I) with Figure 3.1(b.III). The placement of the imperfection can determine the outcome of the folding. For further research, it is, thus, recommended to examine this placement of the imperfections more in detail. While this report has focused more on the quantity of the imperfections and its effects, further research can expand on this model and place the imperfections systematically based on observed terminal hair follicles distributions (or hair patterns) in the abdomen region described in Setty (1966, 1967); Zickler (1997) for both male and female. In order to implement these patterns, however, a solution has to be found to expand the number of nodes on the top surface, allowing for more implemented imperfections and a more realistic model, but without increasing the computational time too much. This report eventually dismissed an even finer mesh on top of the dermis layer due to the increased computational time.

Lastly, the simulation results for the different type of hair distributions (according to the Ferriman Gallwey method, explained in Section 2.3.3), combined with a mean sweat gland distribution, are examined. Based on their initial characteristics, these simulations mimic the biological structure of abdomen skin best. Results, however, did not give any new insights on the effect of skin nonlinearities on excessive skin folding. Foldings on the backside of the structure, as well as in the middle of the structure were found with no noteworthy differences compared to the folding in previous simulations. The only thing worth mentioning is the extreme value for mean curvature for the FG1 score hair distribution (and mean sweat gland distribution) simulation, which has a sharp fold with  $\kappa^* = -5.7$  in the middle of the structure. This is a higher normalized mean curvature compared to earlier findings. Strangely, however, this simulation did not contain any terminal hair follicles. The limited number of available nodes on the top surface resulted in a low output of hair imperfections for the FG1 score distribution, leading to just one vellus hair follicle. No explanation can be given why this simulation resulted in such high curvature, while previously the highest curvature was only visible for models containing the deep terminal hair follicles. Yet again, illustrating that no conclusions can be drawn on the effect of deeper imperfections on the folding.

To conclude this discussion, some general recommendations will be given to continue the work done in this report. Apart from recommendations mentioned earlier in this discussion, further research might consider implementing the *differential growth theory* into the model in agreement with papers done on cortical folding (Garcia et al., 2018; Wang et al., 2021). The shrinking (negative growth rate) of the subcutaneous tissue of the skin (e.g. the hypodermis) is the most reasonable assumption for starting the excessive skin folding. Furthermore, adding gravitational body forces to the model are advised in achieving a more realistic outcome of the model. Lastly, subsequent to the previous recommendations, modeling the dermis layer with a finer mesh (perhaps in millimeter scale) can improve the approximation of the real-life situation as well because simply more nodes can be used for an imperfection. One should, however, compensate for the smaller time increment caused by the finer mesh. This can be done with, for example, mass scaling

(Abaqus/Explicit, 2021), and by increasing the thickness ratio of the dermis and hypodermis layers to prevent mesh crushing while implementing the imperfection.

# Chapter 5: Conclusions

This report gives insight in the influence of skin non-linearities, namely hair follicles and sweat glands, on the excessive skin folding seen in obesity patients after heavy weight loss. The following research question was proposed:

*What are the effects of skin non-linearities, such as hair follicles or sweat glands, on excessive skin folding?*

It was expected that just one imperfection would alter the final morphology of the folding (Garcia et al., 2018; Mavrodontis, 2017). No literature-based hypothesis could be prescribed regarding the question whether depth, or quantity of the imperfections has an additional influence on this folding process.

The results of simulations with one implemented imperfection in Figure 3.1 show that all the types of skin non-linearities cause a folding around the nodal position used for the imperfection. Compared to the control group with no implemented imperfection, the morphology of the top surface folding in the final state has indeed been altered due to the implementation of a skin non-linearity, verifying the hypothesis.

It can, thus, be concluded that the skin non-linearities play a role in the excessive skin folding. However, no convincing difference on the folding has been found regarding different depths, or quantities of the skin non-linearities. At first, results in Figure 3.3 suggested a higher normalized mean curvature  $\kappa^*$  corresponding to the deepest imperfection, namely a terminal (visible) hair follicle penetrating approximately 97% of the dermis skin layer's length. With an extreme value of  $\kappa^* = -3.1$ , the terminal hair showed a higher calculated value for  $\kappa^*$  than the vellus (non-visible) hair follicle and the sweat gland with  $\kappa^* = -2.4$ . However, no difference in normalized mean curvature was found between the vellus hair follicle, and the sweat gland imperfection, while these skin non-linearities do differ in length, and thus, in dermis layer penetration (13% over 49% in). Combined with the fact that an even higher normalized mean curvature of  $\kappa^* = -5.7$  was found in a simulation with no terminal hair follicle imperfection involved (shown in Figure 3.4(b.II)), led to the conclusion that the type of imperfection (or depth of the imperfection) has no effect on the excessive skin folding.

The same conclusion can be drawn for the quantity of imperfections, as Abaqus outputs in Figure 3.4 for average distributed number of hair follicles or sweat glands (based on *in vitro* counts in (Szabo, 1967)) show no different results compared to the single imperfection results in Figure 3.1. This was in terms of number of foldings, and general depth of the foldings. The latter observation is also supported by the fact that no change was visible in  $\kappa^*$ . Furthermore, for all simulations performed (control group, one imperfection, and multiple imperfections) the folding started for the exact same normal, critical pressure  $\sigma_{xx}$  on the dermis layer equal to a value of  $p_{crit}^{sim}$ , approximately equal to an analytically derived critical pressure  $p_{crit}^{ana}$  in Budday et al. (2014).

Thus, skin non-linearities do have an influence on triggering the excessive skin folding process by changing the final morphology of the folding. It has been shown that just a single skin non-linearity can achieve this result. Different depths and quantities of the skin non-linearities showed no different results compared to the single skin non-linearity simulations, meaning no remarks can be made on the vulnerability to excessive skin folding for obesity patients with, for example, a large number of terminal (visible) hair follicles. Folding occurs at approximately the locations of

the implemented skin non-linearity, suggesting a folding behavior dependency on the location of the skin non-linearities. However, not enough data has been generated to support this conclusion.

# Bibliography

- Abaqus/Explicit (2021). *Abaqus reference manuals, Version 6.14*. Dassault Systèmes Simulia Corp, United States. ii, 3, 7, 8, 22
- Annaidh, A. N., Bruyère, K., Destrade, M., Gilchrist, M. D., and Otténio, M. (2012). Characterization of the anisotropic mechanical properties of excised human skin. *Journal of the Mechanical Behavior of Biomedical Materials*, 5(1):139–148. 2
- Atiyeh, B. and Castagliola, M. (2012). *Body Contouring Following Bariatric Surgery and Massive Weight Loss*. Bentham Science Publishers. 3-22. ii, 1
- Bayly, P. V., Okamoto, R. J., Xu, G., Shi, Y., and Taber, L. A. (2013). A cortical folding model incorporating stress-dependent growth explains gyral wavelengths and stress patterns in the developing brain. *Phys Biol*, 10(1):016005. 1
- Björserud, C., Nielsen, C., Staalesen, T., Elander, A., Olbers, T., and Olsén, M. F. (2013). Sahlgrenska excess skin questionnaire (sesq): A reliable questionnaire to assess the experience of excessive skin after weight loss. *Journal of Plastic Surgery and Hand Surgery*, 47(1):50–59. ii
- Budday, S., Steinmann, P., and Kuhl, E. (2014). The role of mechanics during brain development. *J Mech Phys Solids*, 72:75–92. 4, 10, 23
- CAEassistant group (2009). Units in abaqus (1). <https://caeassistant.com/blog/units-in-abaqus-1/>. Accessed: 22-06-2021. 30
- Cotterill, S. (1996). Medical terminology for cancer, chapter 5: The integumentary system (skin). <http://www.cancerindex.org/medterm/medtm5.htm>. Accessed: 21-06-2021. 2
- D’Errico, J. (2021). polyfitn. MATLAB Central File Exchange (<https://www.mathworks.com/matlabcentral/fileexchange/34765-polyfitn>). Accessed: 15-06-2021. 14, 31
- Doll, S., Hauptmann, R., Schweizerhof, K., and Freischläger, C. (1998). Selective reduced integration and volumetric locking in finite deformation elastoviscoplasticity. 5
- Ferriman, D. and Gallwey, J. D. (1961). Clinical Assessment Of Body Hair Growth In Women. *The Journal of Clinical Endocrinology Metabolism*, 21(11):1440–1447. 13
- Garcia, K., Kroenke, C., and Bayly, P. (2018). Mechanics of cortical folding: stress, growth and stability. *Philosophical transactions of the Royal Society of London. Series B, Biological sciences*, 373:20170321. ii, ii, ii, 1, 20, 21, 23
- Hairless NYC Clinic (2014). Vellus hair versus terminal hair. <https://www.hairlessnyc.com/vellus-hair-versus-terminal-hair/>. Accessed: 21-06-2021. 3
- Jain, S., Pandey, K., Lahoti, A., and Rao, P. (2013). Evaluation of skin and subcutaneous tissue thickness at insulin injection sites in indian, insulin naïve, type-2 diabetic adult population. *Indian journal of endocrinology and metabolism*, 17(5):864–870. 20

- Leyva-Mendivil, M. F., Page, A., Bressloff, N. W., and Limbert, G. (2015). A mechanistic insight into the mechanical role of the stratum corneum during stretching and compression of the skin. *J Mech Behav Biomed Mater*, 49:197–219. 1
- Marieb, E. N. and Hoehn, K. (2015). *Human Anatomy Physiology, Global Edition.*, volume Tenth edition. Global edition, pages 150,171,178–179. Pearson. 1, 2, 3
- MATLAB (2021). *version 9.10.0 (R2021a Update 2)*. The MathWorks Inc., Natick, Massachusetts. 14
- Mavrodontis, N. (2017). Buckling, post-buckling imperfections modelled with Abaqus FEA. <https://info.simuleon.com/blog/buckling-post-buckling-imperfections-modelled-with-abaqus-fea>. Accessed: 15-06-2021. ii, 1, 20, 23
- Oomens, C., Brekelmans, M., Loerakker, S., and Baaijens, F. (2018). *Biomechanics: Concepts and Computation*, pages 257–259. Cambridge Texts in Biomedical Engineering. Cambridge University Press, 2 edition. 4, 6
- Oomens, C., van Vijven, M., and Peters, G. (2017). Chapter 16 - skin mechanics. In Payan, Y. and Ohayon, J., editors, *Biomechanics of Living Organs*, volume 1 of *Translational Epigenetics*, pages 347–357. Academic Press, Oxford. 2, 4
- Setty, L. (1966). Varieties of the acuminate abdominal hair pattern of white males. *Journal of the National Medical Association*, 58(3):191–193. ii, 21
- Setty, L. (1967). Varieties of the quadrangular abdominal hair pattern of white males. *Journal of the National Medical Association*, 59(1):45–47. ii, 21
- Shiihara, Y., Sato, M., Hara, Y., Iwai, I., and Yoshikawa, N. (2015). Microrelief suppresses large wrinkling appearance: an in silico study. *Skin Res Technol*, 21(2):184–191. 1, 2, 5, 10, 29
- Song, A. Y., Rubin, J. P., Thomas, V., Dudas, J. R., Marra, K. G., and Fernstrom, M. H. (2006). Body image and quality of life in post massive weight loss body contouring patients. *Obesity*, 14(9):1626–1636. ii, 1, 20
- Spyder Project Contributors (2017). *Spyder 3.1.4, The Scientific PYthon Development EnviRonment*. MIT License (MIT). Created by Pierre Raybaut. 3
- Szabo, G. (1967). The regional anatomy of the human integument with special reference to the distribution of hair follicles, sweat glands and melanocytes. *Philosophical Transactions Of The Royal Society B*, pages 447–485. ii, 12, 21, 23
- Takagi, S. and Tobaru, K. (1954). Notes on the vertical distribution of the human sweat glands. *The Japanese journal of physiology*, 4(3):169–174. 12
- Tallinen, T., Chung, J. Y., Biggins, J. S., and Mahadevan, L. (2014). Gyriification from constrained cortical expansion. *Proc Natl Acad Sci U S A*, 111(35):12667–12672. 1
- Toma, T., Harling, L., Athanasiou, T., Darzi, A., and Ashrafian, H. (2018). Does Body Contouring After Bariatric Weight Loss Enhance Quality of Life? A Systematic Review of QOL Studies. *Obes Surg*, 28(10):3333–3341. ii, 1, 20
- Van Rossum, G. and Drake, F. L. (2009). *Python 3 Reference Manual*. CreateSpace, Scotts Valley, CA. 3
- Wang, S., Demirci, N., and Holland, M. (2021). Numerical investigation of biomechanically coupled growth in cortical folding. *Biomechanics and Modeling in Mechanobiology*. ii, 1, 4, 14, 20, 21

- Wilke, K., Martin, A., Terstegen, L., and Biel, S. S. (2007). A short history of sweat gland biology. *International Journal of Cosmetic Science*, 29(3):169–179. ii, 3, 12
- Wosicka, H. and Cal, K. (2010). Targeting to the hair follicles: Current status and potential. *Journal of Dermatological Science*, 57(2):83–89. ii, 12, 20
- Yildiz, B. O., Bolour, S., Woods, K., Moore, A., and Azziz, R. (2009). Visually scoring hirsutism. *Human Reproduction Update*, 16(1):51–64. 13
- Zickler, R. A. (1997). Sex differences in pubic hair distribution in white population. <https://web.archive.org/web/20110817183921/http://health.tomrue.net/zickler/zickler.htm>. Accessed: 19-06-2021. ii, 21

# Appendix A: Model validations

In the appendices, some of the model validations are shown and explained in more detail, starting with the Von Mises stress comparison of the benchmark model in Appendix A.1

## A.1 Benchmark model: Von Mises stress comparison

In Figure A.1 the Von Mises stress state of the final configuration is shown for multiple simulations varying in both element size and time period of the simulation. Although the color contours differ between the simulations with different element sizes, it still becomes clear that the value for the Von Mises stress is equal regardless of the element size. This cannot be said for the simulations with different time periods, as the 5 and 100 seconds simulations differ in Von Mises stress value from the 10 and 15 second simulations. These time scales are, thus, not time independent. Eventually, as mentioned in Section 2.1.3 in the main text, the process of modelling the benchmark model with multiple elements was continued with an element size of 1000 elements, and a comparison between larger time periods of 25 up until 150 seconds (in steps of 25 seconds).

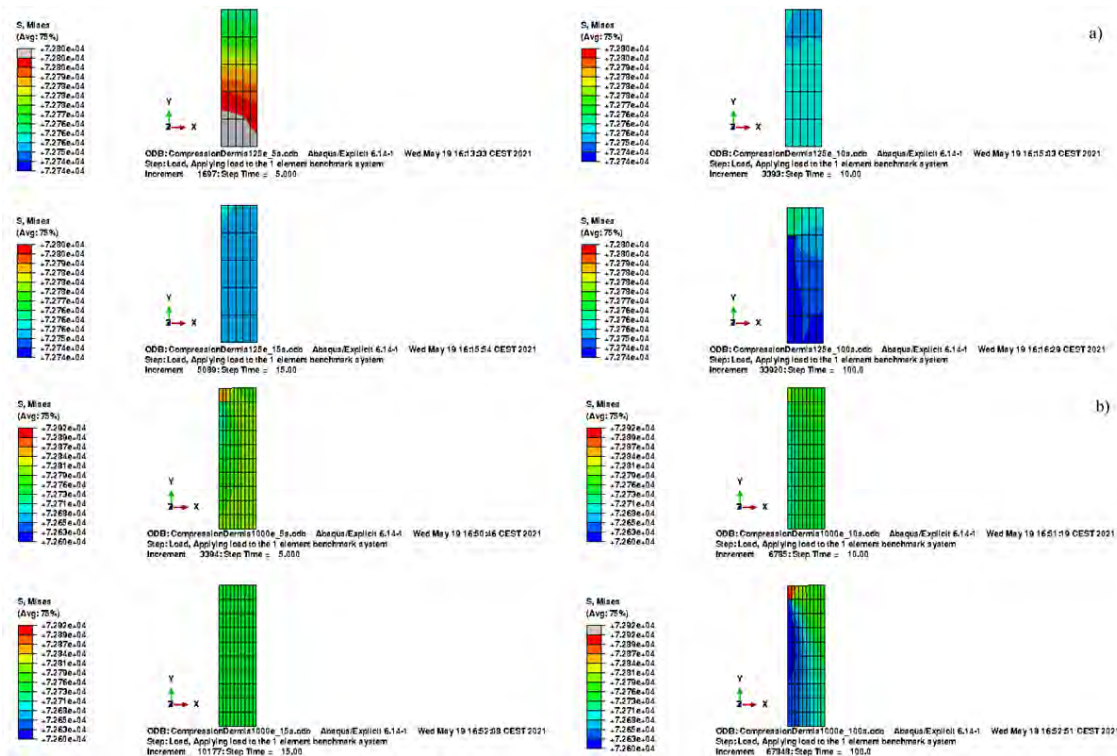


**Figure A.1: Results of the Von Mises stress analysis at the end of both the a) 125 and b) 1000 elements simulation of the dermis skin layer benchmark model. The time periods are shown as follows, starting in the top left corner with 5 seconds, 10 seconds (top right corner), 15 seconds (bottom left corner), and 100 seconds (bottom right corner).**

## A.2 Bi-layered model: Element size check

After implementing the hypodermis into the model, it was decided to change the mesh sizes in both layers. As the interest of this report lies in the folding of the dermis layer, it was decided to apply a finer mesh on this particular layer. To minimize necessary elements in the model, this meant a reduction in the number of elements in the hypodermal layer. To check for the best suitable mesh, some possible mesh sizes were tested in Figure A.2.

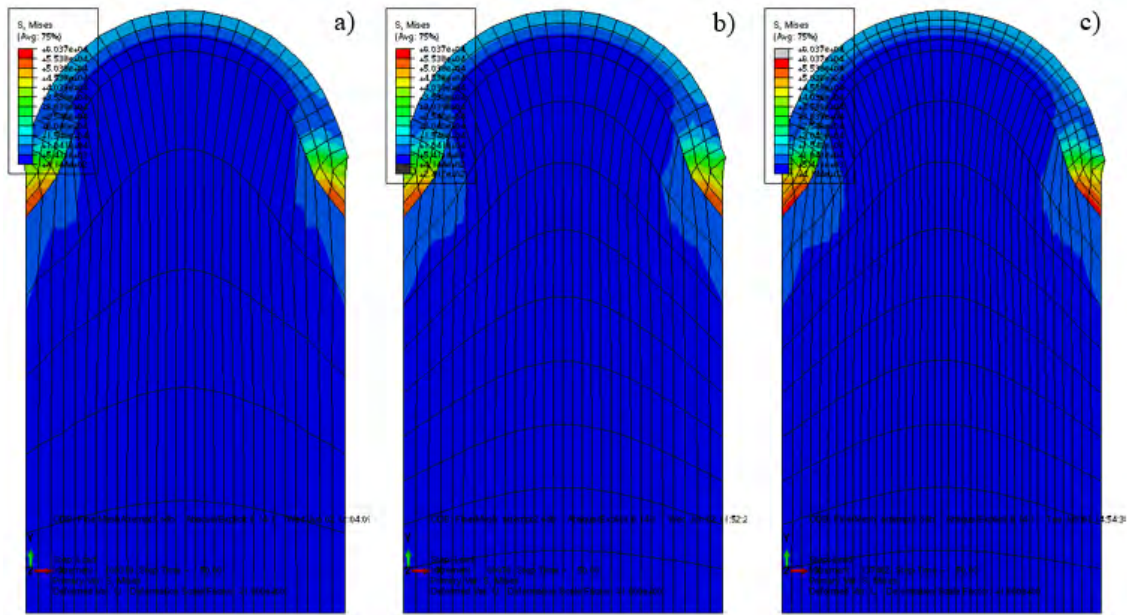


**Figure A.2: Von Mises stress comparison for different element sizes in the bi-layered skin model.** In a) a dermal element size of 0.033 m and a (vertical) hypodermal element size of 0.18 m are used. In b) the element sizes are 0.033 and 0.09 m. Finally, in c) the element sizes are 0.025 and 0.09 m.

Clearly from Figure A.2 the stress state of the bi-layered model is mesh independent. To minimize computational time, the lowest element mesh sizes shown in Figure A.2 were chosen to continue the processing of the model.

## A.3 Bi-layered model: Length scale check

Before implementing the imperfections, and running the final simulations used for the results, a last check was done whether it was possible to translate the models into millimeter scale based on biological skin thicknesses (Shiihara et al., 2015). The model was processed in the meter scale as this provided a suitable computational time to work with. The comparison between the two models is displayed in Figure A.3.

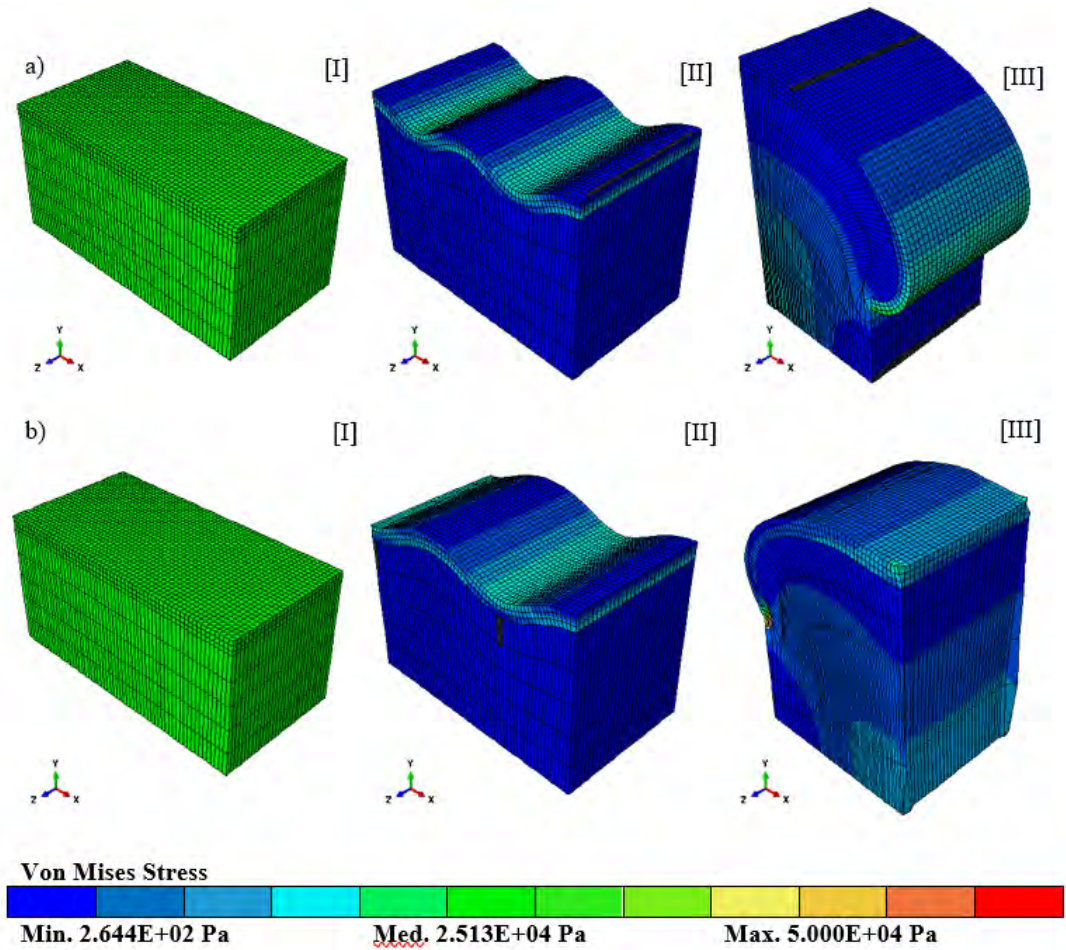


**Figure A.3: Von Mises stress comparison for two models with equal time period, and number of elements, but, different physical length scales (m vs. mm).** Row a) shows the control group simulation of the meter scale model, while row b) shows the same simulation but in millimeter scale (units converted via CAEassistant group (2009)). The states are described by, [I] the initial configuration, [II] the start of the (sinusoidal) folding), and [III] the final state.

It can be seen that the simulations do not have the same morphology in the final configuration. However, the Von Mises stress states are comparable. It was further noticed that the millimeter scale model seems vulnerable to some distortion in the elements at the sides. Furthermore, the meter scale model had a significant faster computational time (2168 over 28868 seconds). All these things considered, it was decided to stick with the meter scale model (despite the different morphologies).

## A.4 Validation of curvature quantification model

The curvature algorithm described in Section 2.4 was first subjected to a model output from the pre-processing stage. Abaqus results of this simulation can be seen in Appendix A.1, namely Figure A.2(a). Based on the definition of the curvature in Section 2.4, positive normalized mean curvatures should dominate in the results of the considered simulation.

First, the functioning of the *polyfitn* (D’Errico, 2021) toolbox in MATLAB was tested by displaying the fitted curve every two hundred iterations. Results of this test for the considered simulation are displayed in Figure A.4.

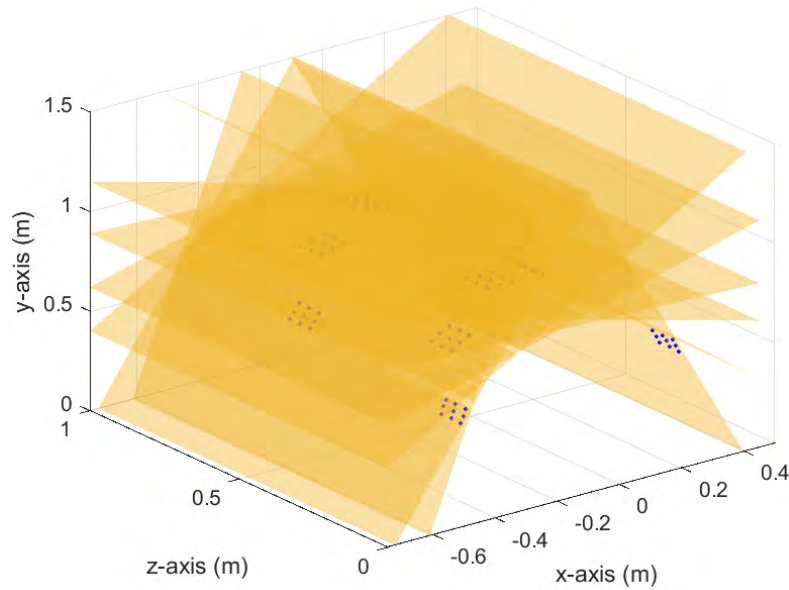


**Figure A.4: Fitted 3D curves using the *polyfitn* function in MATLAB.** Results are shown for the simulation results displayed in Figure A.2(a). The dots represent the eight integration points used for the curve fit.

Although not perfectly visualized in Figure A.4, the *polyfitn* did a sufficient job in fitting the curves. Sequentially, normal vectors outward of these curves were calculated. An additional check of this calculation was done with Figure A.5.

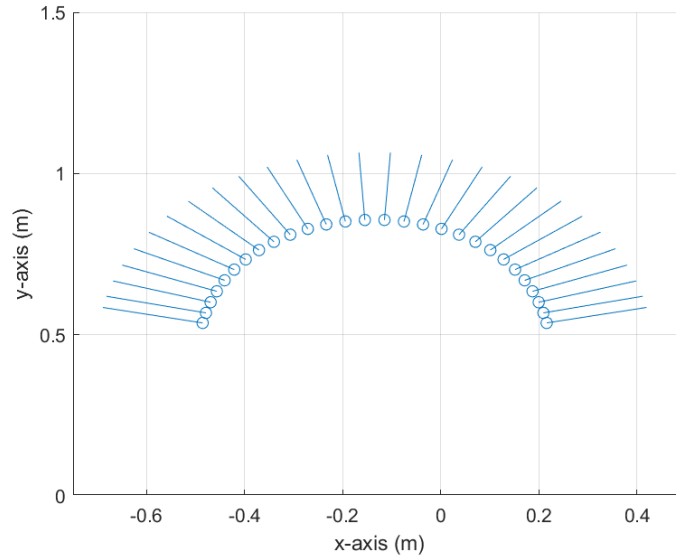


**Figure A.5: Outward normal vectors on the planes visualized in Figure A.4.** The arrows of the vector lie in the  $yz$ -plane. To compensate for that, an additional marker  $o$  was added to show the starting point of the normal vector.

The normalized vectors clearly point in the right direction as we compare the outcome with the Abaqus output in Figure A.2(a). Finally, the normalized mean curvature was calculated along the line  $z = 0.5$  (middle line) in the structure and shown in Figure A.6.

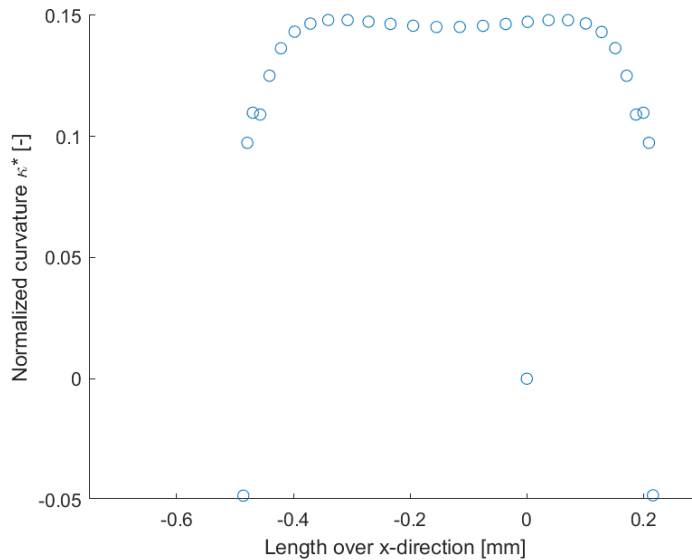


**Figure A.6: Normalized mean curvature calculated for the test simulation**

As stated at the beginning of this Section, positive normalized mean curvatures were expected to be dominant, and that is the case when examining Figure A.6. Thus, the curvature algorithm is validated.